nature materials

SUPPLEMENTARY INFORMATION

https://doi.org/10.1038/s41563-018-0144-z

In the format provided by the authors and unedited.

Robust microscale superlubricity in graphite/hexagonal boron nitride layered heterojunctions

Yiming Song[1,2], Davide Mandelli[3], Oded Hod[3], Michael Urbakh[3], Ming Ma[1,2]* and Quanshui Zheng[2,4]*

[1]State Key Laboratory of Tribology, Department of Mechanical Engineering, Tsinghua University, Beijing, China. [2]Center for Nano and Micro Mechanics, Tsinghua University, Beijing, China. [3]Department of Physical Chemistry, School of Chemistry, The Raymond and Beverly Sackler Faculty of Exact Sciences and The Sackler Center for Computational Molecular and Materials Science, Tel Aviv University, Tel Aviv, Israel. [4]Department of Engineering Mechanics, Tsinghua University, Beijing, China. *e-mail: maming16@tsinghua.edu.cn; zhengqs@tsinghua.edu.cn

Robust Microscale Superlubricity in Graphite/Hexagonal Boron Nitride Layered Heterojunctions

Supplementary Information

Yiming Song,[1,2] Davide Mandelli,[3] Oded Hod,[3] Michael Urbakh,[3] Ming Ma,[1,2*] Quanshui Zheng[2,4*]

1) State Key Laboratory of Tribology, Department of Mechanical Engineering, Tsinghua University, Beijing 100084, China.

2) Center for Nano and Micro Mechanics, Tsinghua University, Beijing 100084, China.

3) Department of Physical Chemistry, School of Chemistry, The Raymond and Beverly Sackler Faculty of Exact Sciences and The Sackler Center for Computational Molecular and Materials Science, Tel Aviv University, Tel Aviv 6997801, Israel.

4) Department of Engineering Mechanics, Tsinghua University, Beijing 100084, China.

In this supplementary information, we provide additional details on certain aspects of the study reported in the manuscript. The following issues are discussed:

1. **Normal Force Dependence in the High Friction State**

In Fig. 4a of the main text we presented the dependence of the measured frictional-stress on the applied normal load at a misaligned interfacial orientation. For completeness, we present in Fig. S1 a similar dependence for the aligned interface demonstrating that even in the higher-friction configuration the frictional-stress of the heterogeneous junction is nearly independent of the applied load up to 100 μN. The corresponding friction coefficient at the aligned configuration is estimated to be smaller than 5.9×10^{-3}.

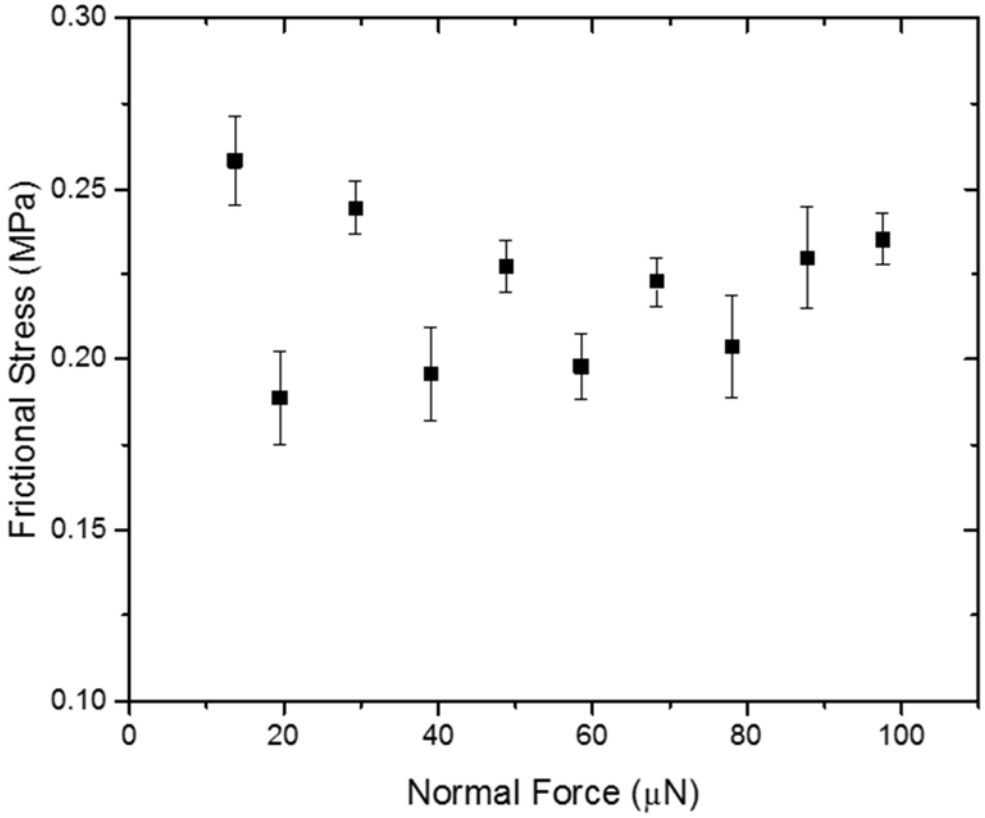

Figure S1: Load dependence of the frictional-stress between untreated aligned monocrystalline graphite and *h*-BN surfaces at sliding velocity of 600 nm/s and under ambient conditions (temperature of 28.5±0.5 ºC and relative humidity of 53.6±1%).

2. **Reproducibility of the Measurements of Anisotropic Friction**

To verify the reproducibility of the measured frictional-stress anisotropy between graphite and *h*-BN presented in the main text, we repeated our measurements with another sample scanning an angular range of ~120°. As shown in Fig. S2, the angular dependence of the measured friction stress of the second sample exhibits two peaks of height ~0.12 MPa separated by ~60°, in agreement with

the results presented in Fig. 2 of the main text. We further compare in panels (b) and (c) of Fig. S2, respectively, the lateral shear-stress loop measured for the aligned contact (red circle in Fig. S2a) to that of a misaligned contact (blue circle in Fig. S2a). Clearly, the frictional stress, evaluated as the average shear-stress measured over several such 2 μm loops, is higher for the aligned contact.

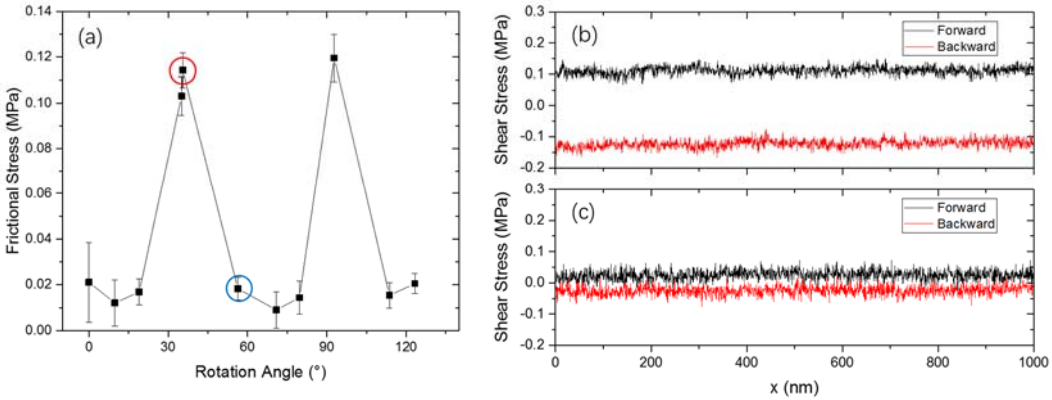

Figure S2: Demonstration of the reproducibility of the anisotropic friction measured between graphite and *h*-BN. (a) Dependence of the measured frictional-stress on the relative orientation between the second sample of monocrystalline graphene and *h*-BN surfaces under ambient condition. Lateral shear-stress loops corresponding to the aligned contact (see red circle in panel (a)) and a misaligned contact (see blue circle in panel (a)) are presented in panels (b) and (c), respectively. Here, forward traces are marked in black and backward traces are marked in red.

3. Experimental Error Sources

In our experiments, there are four measured quantities including: (i) the interlayer rotation angle; (ii) the sliding velocity; (iii) the applied normal force; and (iv) the lateral force.

The rotation angle is controlled by driving the graphite flake using an AFM tip. Its value is measured visually based on images taken under an optical microscope. For each image, we performed multiple measurements (e.g. 5 times) and estimated the error from the variation of the results. The resulting error was found to be ~0.5°, which is too small to be resolved in Fig. 2 of the main text.

The sliding velocity is controlled by driving the AFM stage using a piezoelectric ceramic transducer (PZT) with close-loop feedback at a given value. The precision of the displacement induced by the PZT is 0.4 nm, with a typical scanning duration ~0.2 sec, the corresponding estimated error in the reported velocity is 2 nm/s, which is about 3% of the lowest sliding velocity (60 nm/s) considered. By measuring the displacement as a function of time, one can further provide an independent estimation of the error (see Fig. S3). For example, after setting the desired velocity to be

60 nm/s, we measured the displacement of the stage as a function of time as shown below, a linear fitting shows that the velocity measured is 60.32±0.03 nm/s. This constitutes an error of 0.5% with respect to the set velocity.

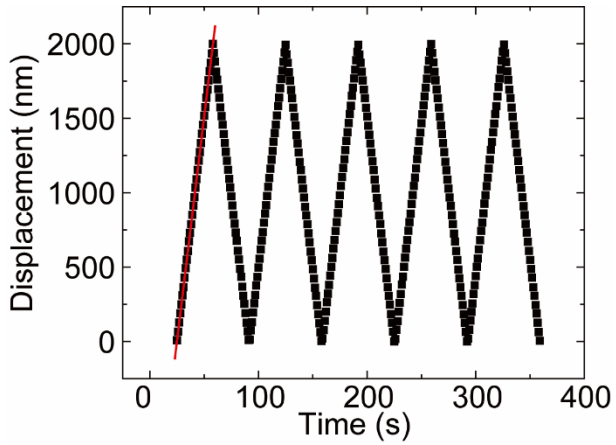

Figure S3: Displacement of the AFM stage as a function of time measured experimentally. The solid line represents the linear fitting.

The normal force is applied using the AFM cantilever, for which the largest source of error would be the calibration step. With a given optical detector signal I_n, the normal force F_n is given by

$$F_n = k_n \times S_n \times I_n, \tag{S1}$$

where S_n is the optical lever sensitivity and k_n is the normal spring constant. The lever sensitivity is measured by performing a standard force curve measurement,[1] where the AFM tip approaches the SiO_2 surface until a certain deflection of the cantilever is reached and then retracts. During such process, the displacement of the AFM stage along the z direction u_z and the photodiode detector current representing vertical deflection I_{dfl} are recorded. The slope of u_z as a function of I_{dfl} gives S_n. By performing the force curve measurements for 6 times, the standard deviation of S_n in our experiments, ΔS_n, is estimated to give $\langle \Delta S_n / S_n \rangle \leq 0.005$. By recording the I_n signals with the cantilever being in its free state for 4 times, the standard deviation of I_n in our experiments ΔI_n is estimated to give $\langle \Delta I_n / I_n \rangle \leq 0.0093$.

The normal spring constant k_n is calibrated by the Sader method.[2] We notice that this method is strictly valid only for rectangular cantilevers,[1] which is different from the shape of the cantilever we used (NT-MDT VIT-P). To verify the validity of the method in our case, we used the reference cantilever method[3, 4] as a cross check. For the cantilever used in experiments, the error ε_n is defined as[5]

$$\varepsilon_n = \frac{{k_n}^{(Sader)} - {k_n}^{(Ref)}}{{k_n}^{(Sader)} + {k_n}^{(Ref)}}, \tag{S2}$$

where ${k_n}^{(Sader)}$ is 43.91 N/m estimated from Sader method, ${k_n}^{(Ref)}$ is 35.99 N/m estimated from reference cantilever method leading to a value of $\varepsilon_n = 9.9\%$ for the estimated spring constant error. The evaluation of the overall error in the normal force as a function of its individual constituent contributions is discussed below along that of the lateral force.

Similar to the normal load, the largest source of error for the lateral force, applied using the AFM tip, is also the calibration step. The lateral force F_l is given by

$$F_l = \alpha \times I_l, \tag{S3}$$

where $\alpha = k_l \times S_l$, k_l being the lateral spring constant, S_l is the lateral optical lever sensitivity, and I_l is the photodiode detector current representing lateral deflection. We used the wedge method[6, 7] to obtain α. This method is widely used as an experimental reference technique.[8] We also used the diamagnetic lateral force calibration method[9] to estimate the error, for cross checking.

The error for α is given by

$$\varepsilon_\alpha = \frac{\alpha^{(Wedge)} - \alpha^{(DFLC)}}{\alpha^{(Wedge)} + \alpha^{(DFLC)}} \tag{S4}$$

With $\alpha^{(Wedge)}$ being 34.26 μN/nA estimated from the wedge method, $\alpha^{(DFLC)}$ being 25.68 μN/nA estimated using diamagnetic lateral force calibration method. The resulting estimated error in α is $\varepsilon_\alpha = 14.3\%$. By recording the I_l signals with cantilever in its free state for 6 times, the standard deviation of I_l in our experiments ΔI_l is estimated to give $\langle \Delta I_l / I_l \rangle \leq 0.197$.

To estimate the overall error in the reported normal and lateral forces we assume that the errors of their different constituents, appearing in Eqs. (S1) and (S3), are small, uncorrelated and without systematic offset. Under these conditions, the estimated variance of a general function of several parameters $f(x_1, \ldots, x_n)$ is given by:

$$\sigma_f^2 = \sum_i \left(\frac{\partial f}{\partial x_i}\right)^2 \sigma_i^2 \tag{S5}$$

where σ_i and σ_f are the standard deviations of x_i and f, respectively. Applying the general expression of Eq. (S5) to the normal and lateral forces given by Eqs. (S1) and (S3) yields:

$$\left(\frac{\Delta F_n}{F_n}\right) = \sqrt{\left(\frac{\varepsilon_n}{k_n}\right)^2 + \left(\frac{\Delta S_n}{S_n}\right)^2 + \left(\frac{\Delta I_n}{I_n}\right)^2} = 9.96\% \tag{S6}$$

and

$$\frac{\Delta F_l}{F_l} = \sqrt{\left(\frac{\varepsilon_\alpha}{\alpha}\right)^2 + \left(\frac{\Delta I_l}{I_l}\right)^2} = 24.34\%. \tag{S7}$$

The measurement errors estimated above match well the standard deviation of the frictional-stress obtained from 16 independent frictional measurements that set the error bars appearing in the experimental diagrams of the main text.

4. **Surface Characterization**

In the Methods section we describe several procedures we used to evaluate the quality of the sliding surfaces. The figures presented below relate to that section.

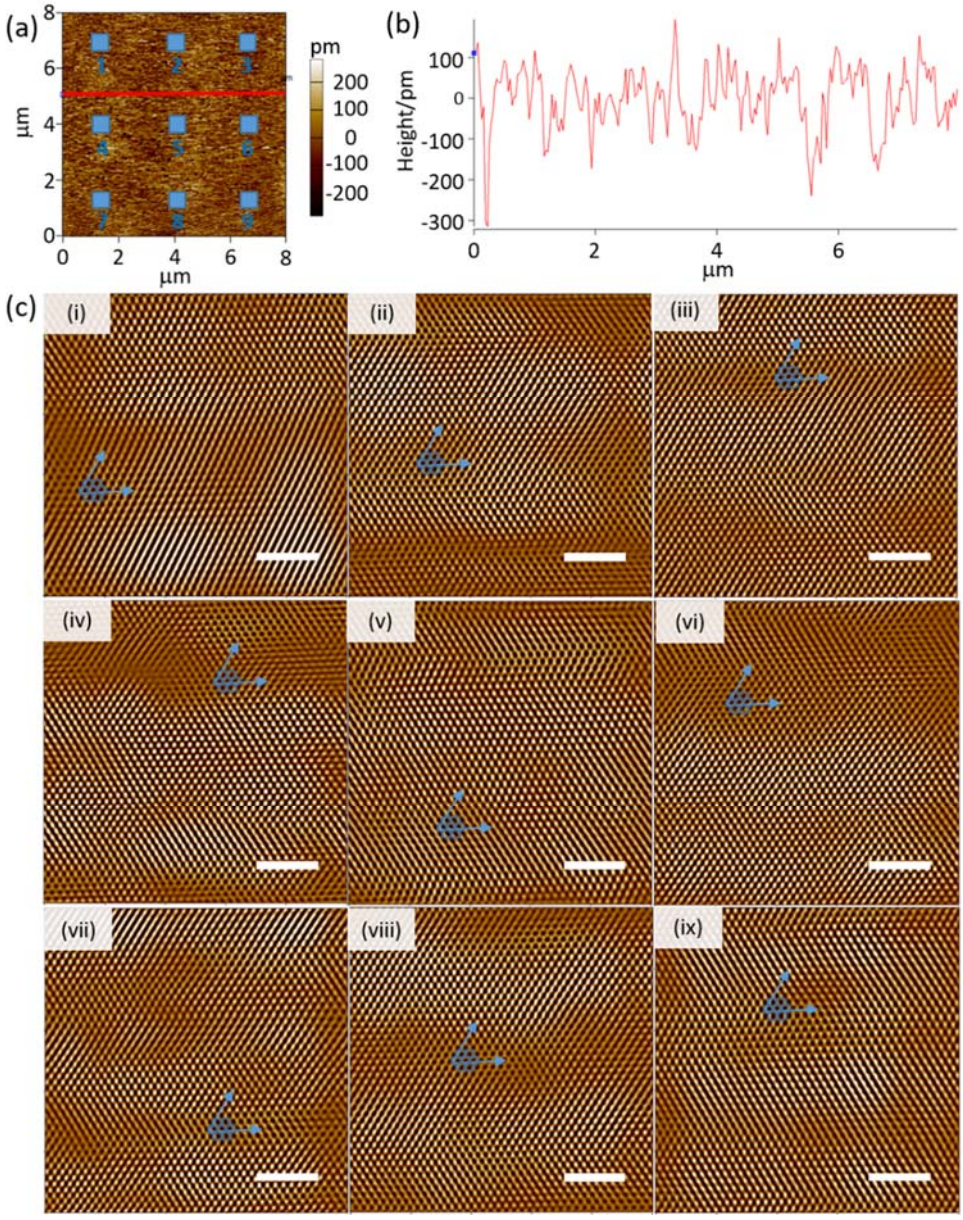

Figure S4: AFM characterization of the *h*-BN substrate surface roughness and mono-crystallinity. (a) AFM height image of the smooth *h*-BN substrate region used in the friction measurements. The nine 10×10 nm^2 spots used to verify the

surface mono-crystallinity are marked by light-blue squares; (b) *h*-BN surface roughness profile measured along a specific scan-line marked by the solid red line in panel (a); (c; i-ix) Atomically resolved AFM images of the nine spots shown in panel (a). The identical crystal orientation of all spots strongly indicates the mono-crystallinity of the smooth substrate region used in the friction measurements. All scale bars correspond to a length of 2 nm. The imposed wavy pattern is caused by the scanning noise of the AFM apparatus.

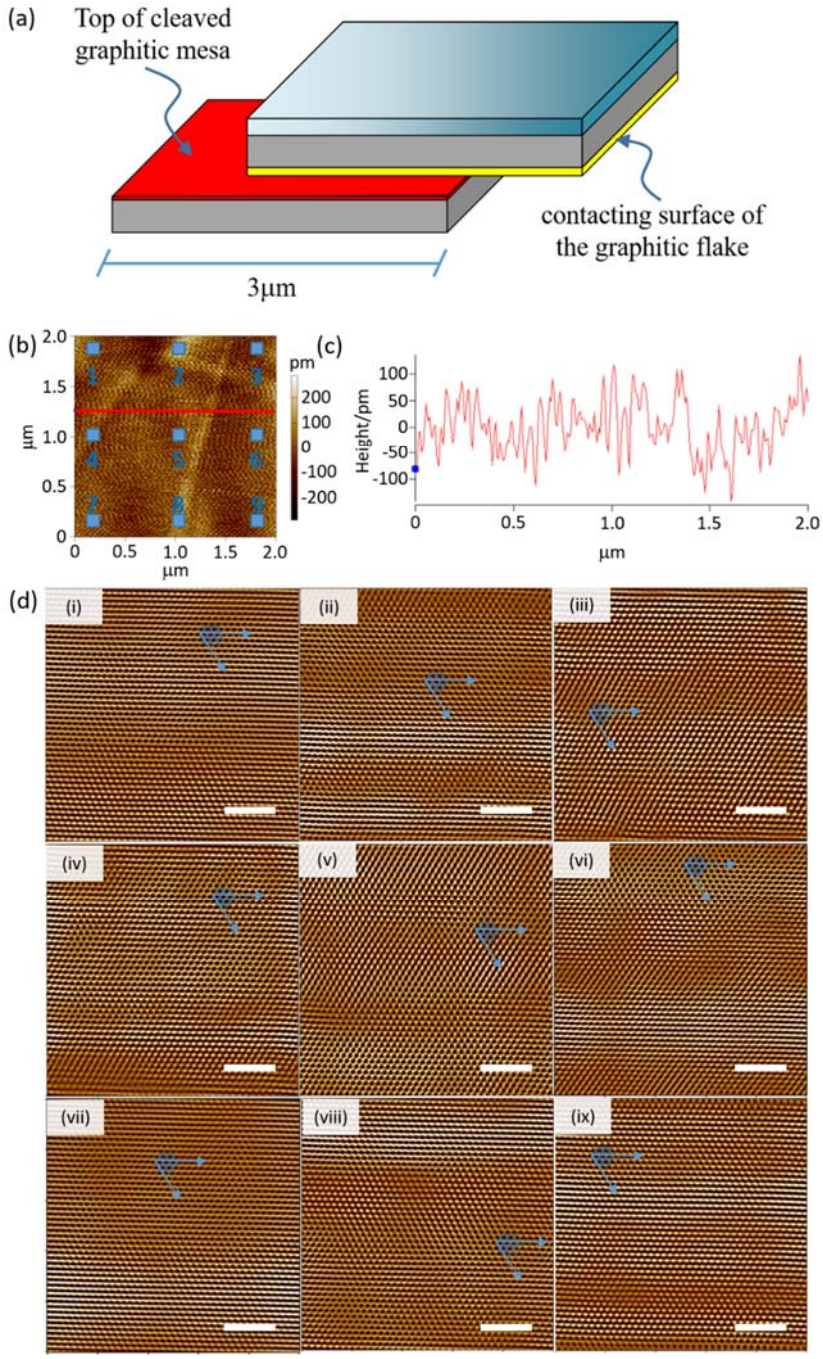

Figure S5: AFM images of a cleaved upper graphitic mesa surface. (a) A schematic representation of the cleaved mesa and the sheared flake that is later transferred atop the *h*-BN surface. The top surface of the cleaved mesa and the contacting surface of the flake are marked in red and yellow, respectively; (b) AFM height image of the upper surface of the cleaved

graphitic mesa. The nine 10 × 10 nm^2 spots used to verify the surface mono-crystallinity are marked by blue squares; (c) Graphite surface roughness profile measured along a specific scan-line marked by solid red line in panel (b); (d, i-ix) Atomically resolved AFM images of the nine spots shown in panel (b). The identical crystal orientation of all spots strongly indicates the mono-crystallinity of the graphitic surface used in the friction measurements. All scale bars correspond to a length of 2 nm. The imposed wavy pattern is caused by the scanning noise of the AFM apparatus.

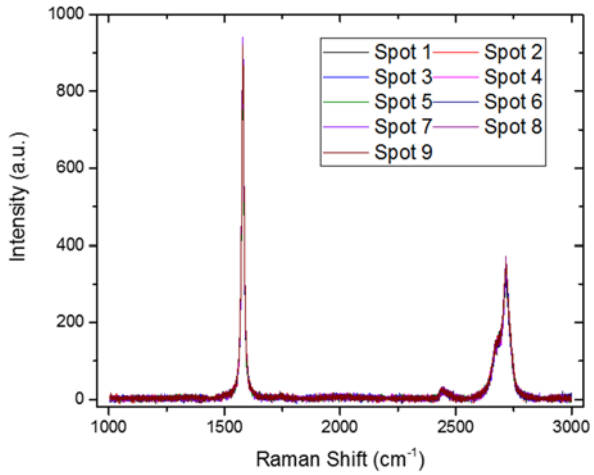

Figure S6: Raman spectra collected over the 9 selected spots across the surface of the cleaved graphitic mesa shown in Fig. S5b. The absence of the characteristic D-peak at 1,350 cm^{-1} in all the measured spectra indicates the high degree of surface crystallinity.

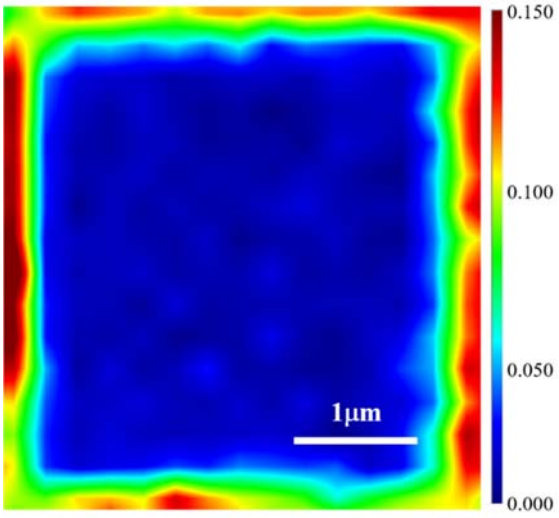

Figure S7: I_D/I_G Raman image of the top surface of the cleaved graphite mesa. I_D and I_G are the intensities of the D and G peaks, respectively.[10] The spacing of the square array was set to 0.25 μm to ensure overlap between adjacent laser spots. The overall scan area was ~16 μm^2. The region with low I_D/I_G (blue color region in the center) indicates a nearly defect free surface.[11]

Figure S8a is an enlarged version of the height profile image Fig. S5b above showing a possible step in the cleaved graphitic surface. To evaluate the nature of this apparent step we analyzed the in situ friction force measured across it (Fig. S8b) showing no enhancement of friction. This indicates that the step is an internal (buried) step as illustrated in Fig. S8c[12]. This is also supported by the ID/IG Raman image (Fig. S7) showing a nearly defect free surface. From Figs. S5b and S5c, we can estimate the slope induced by this internal step to be merely 0.2°, indicating a nearly flat surface thus further supporting the uniform friction map.

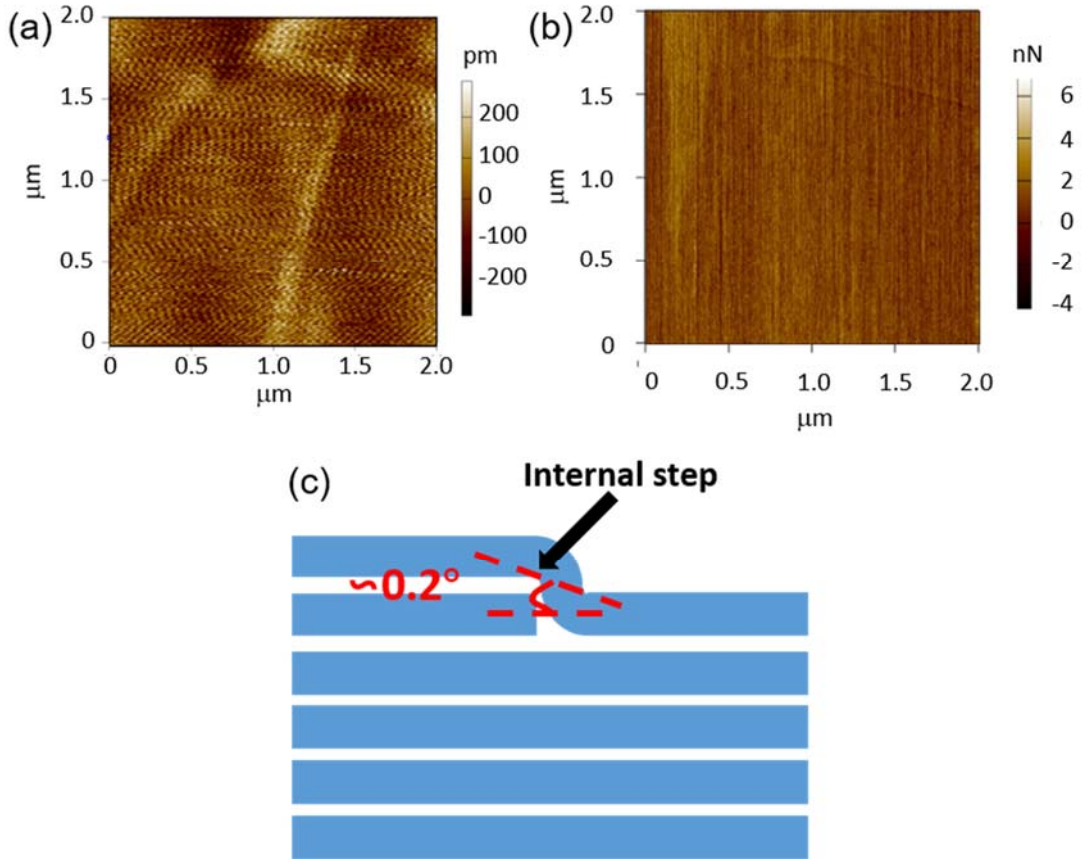

Figure S8: (a) AFM height image of the upper surface of the cleaved graphitic mesa. (b) AFM friction force map measured between the AFM tip and the upper surface of the cleaved graphitic mesa. (c) Schematic diagram of an internal graphitic step.

5. **Characterization of the AFM Tip and Pressure as well as Relative Slip Estimation**

As described in the Methods section, to enable a relatively large contact area between the tip (whose original radius was ~10 nm) and the SiO_2 cap of the graphite mesa, prior to the friction measurements a relatively large normal force of ~100 μN was intentionally applied to induce a plastic deformation of the tip. The scanning electron microscope image of the deformed tip is shown in Fig. S9a, clearly demonstrating the flattening of the tip and increase of its contact radius to ~0.5 μm. Compared to the 3×3 μm^2 surface area of the graphite slider this suggests that some pressure gradient may still develop across the frictional interface. Nevertheless, one should consider the multi-layer nature of the slider and the silicon oxide cap that comes in contact with the tip. These may serve as buffer layers that spread the load more evenly across the interface.

To get an approximate estimation of the normal load distribution induced by the flattened tip at the graphite/*h*-BN interface we adopted the continuum elastic theory model for a transversely isotropic semi-infinite medium presented in Ref.[13]. Considering a normal force applied uniformly across an area of (tip) radius, $R = 0.5\mu m$, at the surface of a semi-infinite graphite substrate, we computed the normal stress distribution $\sigma_{zz}(x, y)$ at a depth of $1.2\ \mu m$ below the surface, which corresponds to the thickness of the experimental SiO_2 capped graphite flake (including the SiO_2 buffer layer itself). In the calculations the following values of the elastic constants of graphite, C_{11}=958.17, C_{12}=346.90, C_{13}=-1.30, C_{33}=35.46, C_{44}=2.73, C_{66}=306.89 GPa, have been used. These were obtained from a quadratic fit of the energy versus strain curves of a bulk graphite model simulated adopting the REBO intra-layer potential, and the Kolmogorov-Krespi inter-layer potential[14, 15]Since the elastic properties of bulk *h*-BN are similar to those of graphite, our approximation that considers a homogeneous graphitic block is expected to be a sufficiently good representation of the heterojunction as well. The calculated relative deviations of the normal stress from its average value computed across a contact area of $3 \times 3\ \mu m^2$ that corresponds to the size of the experimentally measured graphite flake are presented in Fig. S9b. We found a maximal 6-fold deviation of the normal stress from its average value, suggesting that the experimental SiO_2 capped graphite slider effectively spreads the applied normal load more evenly across the contact area.

Importantly, our experiments demonstrate that the frictional stress is basically unaffected by two order of magnitudes variations in the applied normal load. This further suggests that the non-uniform load distribution induced by the finite size of the tip should have a negligible effect on the friction.

Furthermore, keeping in mind the strong van der Waals adhesion between the atomically flat graphite and *h*-BN surfaces, it is reasonable to assume full contact between the surfaces.

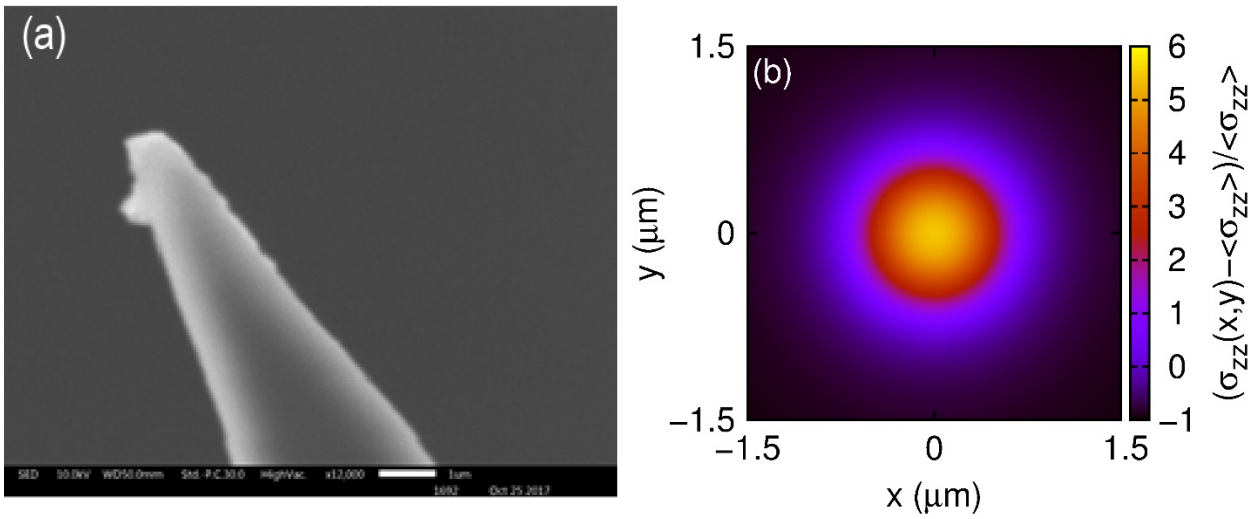

Figure S9: (a) SEM image of the AFM tip after the induced plastic deformation. (b) Estimation of the normal load distribution at the graphite/*h*-BN interface.

In order to verify that there is no slip between the tip and the SiO_2 cap, we measured the friction between the AFM tip (VIT-P tip, NT-MDT, Russia) and a SiO_2 surface, which was processed following the same procedure used for preparing the SiO_2 cap on the graphitic flakes. Figure S10a below shows a typical friction loop measured with a normal load of ~19.7 μN and a sliding speed of 200 nm/s under ambient condition. The friction loop includes four stages. For the forward trace the AFM tip initially twists (see Fig. S10b,c) without relative translational displacement with respect to the SiO_2 surface (stage (i) in Fig. S10a). When the lateral force exceeds a critical value (~10000 nN), corresponding to the static friction force, the tip starts sliding atop the SiO_2 surface (stage (ii) in Fig. S10a). Similar stages occur for the backward trace (stages (iii) and (iv)). Compared with the friction between graphite and *h*-BN under the same condition, the static friction between tip and SiO_2 is 7 times larger. Therefore, there is no slip between tip and SiO_2. In order to further eliminate the effect of tip twisting on the measured friction we have considered measurement results obtained only during the steady-state motion corresponding to stages (ii) and (iv) in Fig. S10a.

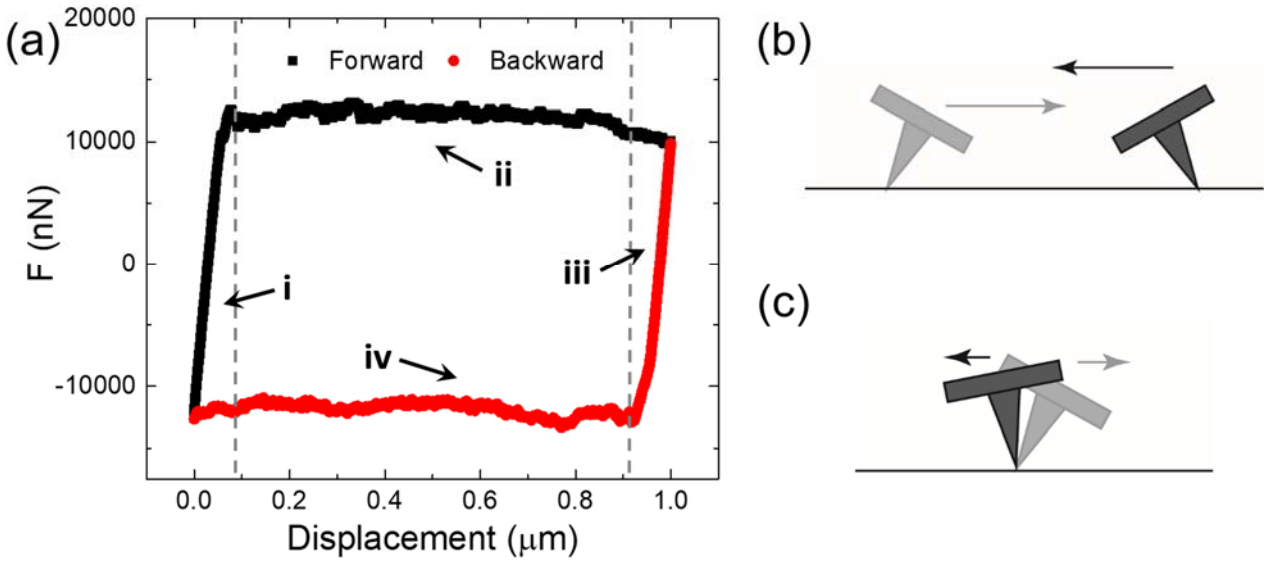

Figure S10: (a) Friction loop measured between the AFM tip and a SiO_2 surface. (b) and (c) provide illustration of the AFM tip sliding on the SiO_2 surface during stages ii, iv and i, iii, respectively. The measured friction outside of the vertical dashed lines in panel (a) is ignored[4].

6. Frictional-Stress Anisotropy for the Homogeneous Graphene Interface

In Fig. 3b of the main text we presented the instantaneous shear-stress calculated for the aligned homogeneous graphitic contact (black line). To demonstrate the large orientational anisotropy of the frictional-stress in this case we compare it (Fig. S11a) to the shear-stress obtained for the 30° rotated counterpart (Fig S11b). While the aligned homogeneous contact exhibits strong stick-slip motion, the misaligned junction reaches smooth sliding after ~1 ns with minor fluctuations of ~0.05% around the average value, for the chosen simulation parameters. Figure S11c reports the calculated time-averaged frictional-stress as a function of the orientational misfit angle, θ. A small misalignment of only ~1° away from θ=0° already results in a decrease of two orders of magnitude in the kinetic frictional-stress. The overall anisotropy factor between the aligned and 30° rotated junctions is ~600, as reported in the main text.

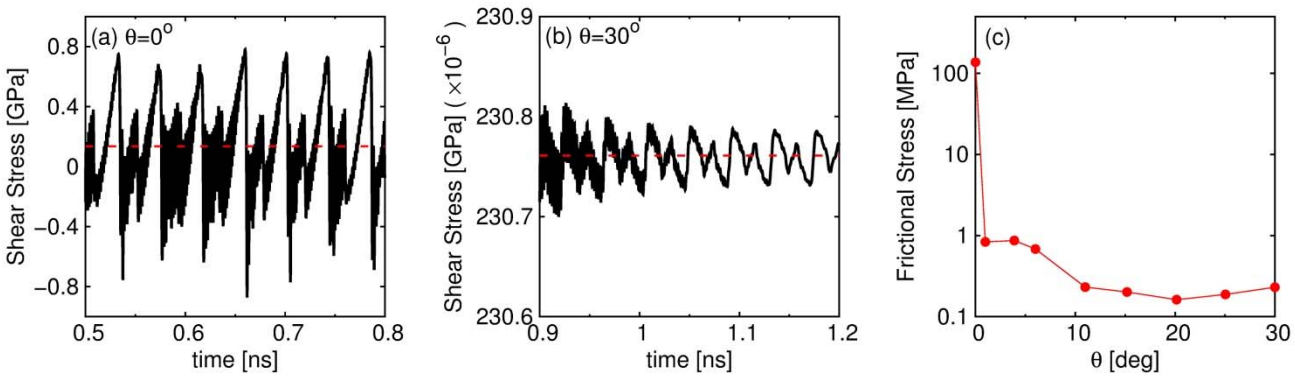

Figure S11: Simulated shear-stress traces in the (a) aligned (θ=0°) and (b) misaligned (θ=30°) homogeneous graphene/graphene interface. The red dashed lines correspond to the average kinetic frictional-stress. (c) The average kinetic frictional-stress calculated in the homogeneous junction as a function of the misalignment θ. The simulations were performed using uniform stage/graphene spring constants of $K_{\parallel} = 11\ \mathrm{meV/Å^2}$ and a driving velocity of $\mathrm{v_{stage}} = 10\ \mathrm{m/s}$. The damping coefficients are chosen as $\eta_z = 4.425\ \mathrm{ps^{-1}}$ and $\eta_x = \eta_y = 0.029\ \mathrm{ps^{-1}}$.

7. Effects of Thermal Fluctuations on the Simulation Results

In the main text, we reported results obtained from simulations conducted at zero temperature, $\mathrm{T} = 0$ K. To study the effects of thermal fluctuations on the calculated frictional properties we have repeated the calculations at finite temperature adopting a standard Langevin approach for the same model including a graphene layer sliding over a rigid *h*-BN substrate. The equations of motions of all carbon atoms within the slider are given by:

$$\mathrm{m_C}\ddot{\mathrm{r}}_\mathrm{i} = -\nabla_{\mathrm{r_i}}\left(\mathrm{V_{inter}^{ILP}} + \mathrm{V_{intra}^{REBO}}\right) + K_{\parallel}\left(\mathrm{r_{\parallel,i}^{stage}} - \mathrm{r_{\parallel,i}}\right) + \sum_{\alpha=\mathrm{x,y,z}}\left(\zeta_\alpha \mathrm{R(t)} - \mathrm{m_C}\eta_\alpha \mathrm{v_{\alpha,i}}\right)\hat{\boldsymbol{\alpha}},$$

where $\mathrm{R(t)}$ is a delta-correlated stationary Gaussian process, namely $\langle \mathrm{R(t)} \rangle = 0$, and $\langle \mathrm{R(t)R(t')} \rangle = \delta(\mathrm{t} - \mathrm{t'})$. The coefficients $\zeta_\alpha = \sqrt{2\mathrm{m_C}\eta_\alpha \mathrm{k_B T}}$ satisfy the fluctuation-dissipation theorem.

The frictional stress is computed adopting the following protocol. First, we equilibrated the graphene layer connected by springs to the rigid support, at rest. The latter was then set into motion at constant velocity for a total duration of 10 ns. We discarded the initial transient and computed the average frictional stress obtained at steady state. We studied two misfit angles of $\theta = 0^0$ and $\theta \simeq 30^0$, and two temperatures, $\mathrm{T} = 10$ and 300 K. All other simulation parameters were the same as those used for performing the simulations at $\mathrm{T} = 0$ K.

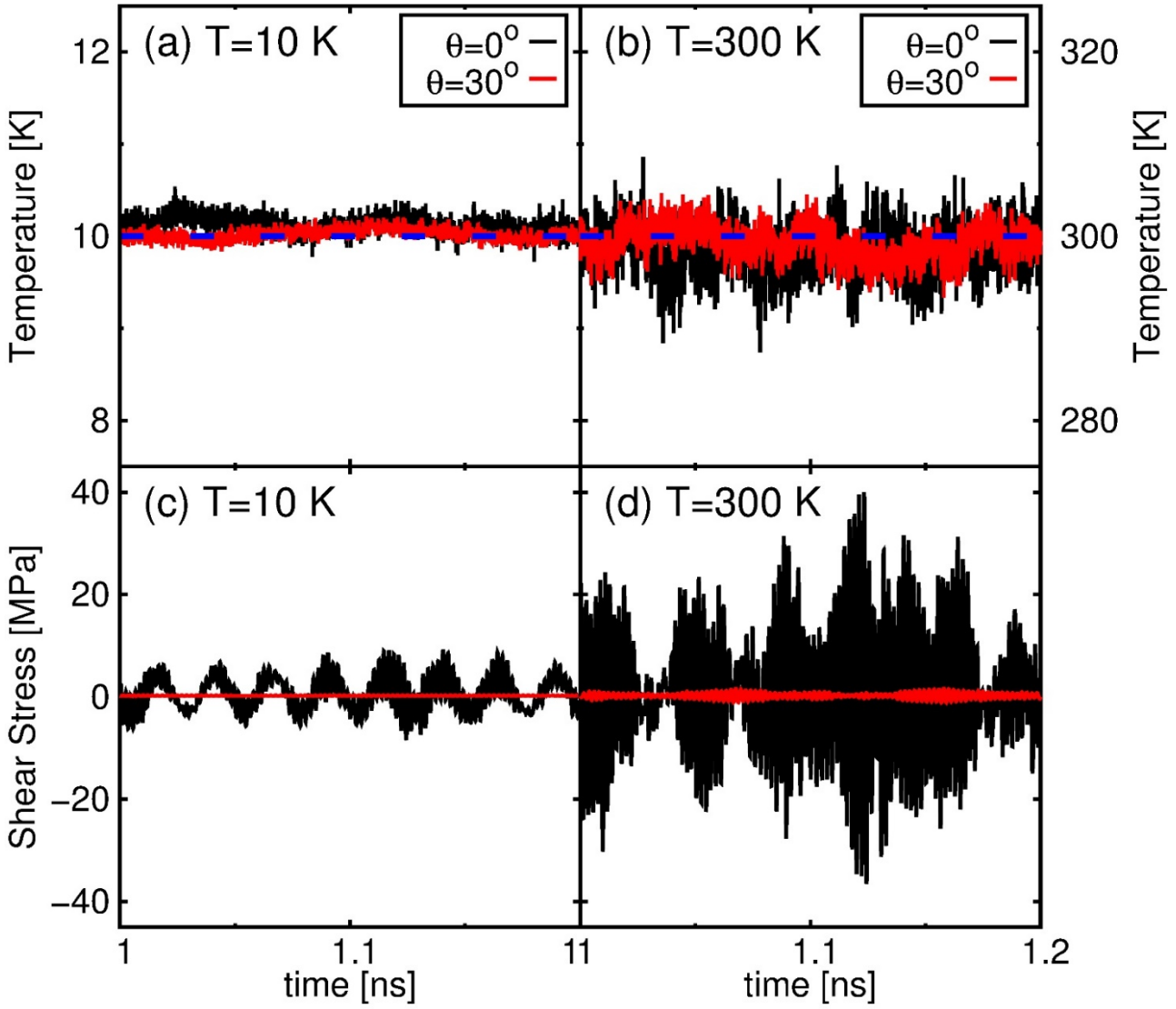

Figure S12: Trajectories from the sliding friction simulations of the heterogeneous graphene/*h*-BN interface performed at finite temperature. Panels (a) and (b) report the instantaneous temperature measured during sliding of the aligned (black curves) and thirty degrees rotated (red curves) interfaces, during simulations performed at finite temperatures of 10 and 300 K, respectively. The blue dashed line is the temperature of the applied Langevin thermostat. Panels (c) and (d) report the corresponding friction traces.

Figures S12a,b show the graphene layer's instantaneous temperature, calculated from the kinetic energy per atom (ε_{kin}) as $T = 2\varepsilon_{kin}/3k_B$, along the sliding trajectories of the aligned and rotated interfaces, at a thermostat temperature of 10 and 300 K, respectively. The instantaneous temperatures (full black and red lines) fluctuate around the thermostat temperature (dashed blue line) indicating the validity of the used procedure. Figures S12c,d report the corresponding steady-state friction trace. At low temperature (10 K) the fluctuations are relatively small and the friction trace of the aligned contact shows an oscillatory behavior with period of ~2.4 ps, which translates to a displacement of

$\Delta x \simeq 2.4$ Å $\approx a_{h-\mathrm{BN}}$ of the moving stage, corresponding to the lattice spacing of the substrate (see full black line in Fig. S12c). At 300 K, thermal fluctuations mask this periodic behavior (see full black line in Fig. S12d). Notably, despite the increase in the force fluctuations with increasing bath temperature we observe only a mild increase in the average frictional stress, as shown in Fig. S13a accompanied by a mild increase of the overall frictional orientational anisotropy as reported in Fig. S13b.

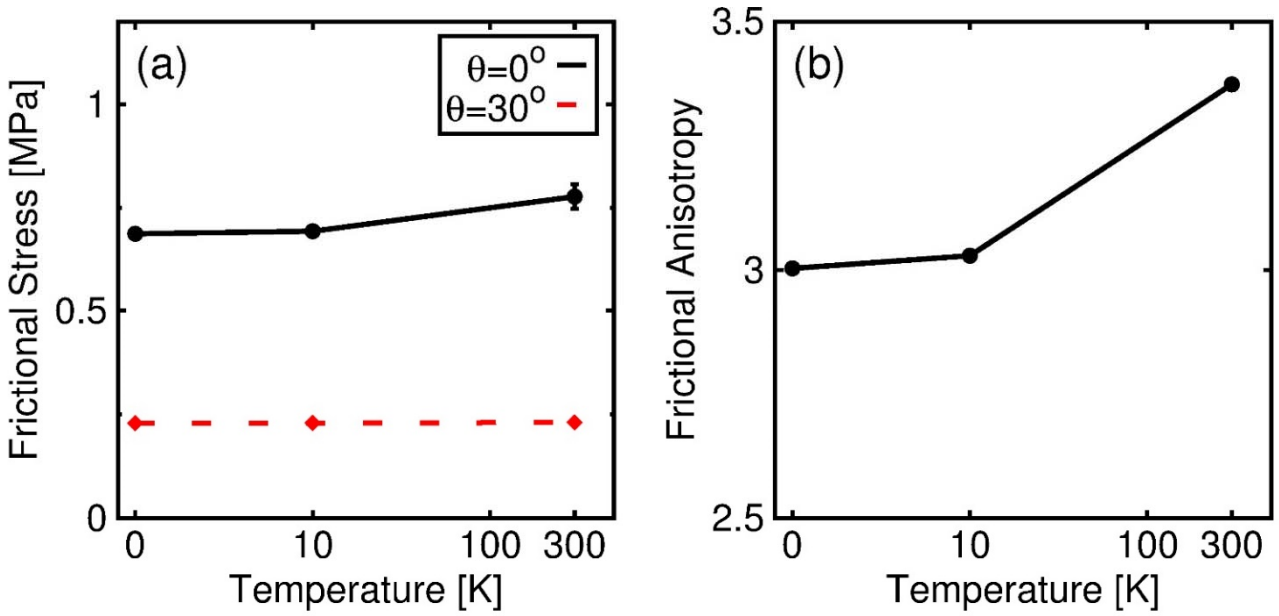

Figure S13: Temperature dependence of the frictional stress in the heterogeneous graphene/*h*-BN interface. Panel (a) shows the average frictional stress as a function of temperature in the aligned (solid black curve) and thirty degrees rotated (dashed red curve) heterojunction. Panel (b) reports the corresponding frictional anisotropy, calculated at each temperature as the ratio between the average frictional stresses measured at $\theta = 0^0$ and $\theta \simeq 30^0$. Error bars related to the thermal averaging are typically smaller than the mark size.

The weak temperature dependence of the frictional anisotropy originates from the robustness of the structural properties of the moiré pattern at the incommensurate contact. We quantify this observation by computing the global registry index (GRI)[16] at different temperatures. The GRI quantifies the degree of interfacial commensuration via a single number attaining values between zero and one, where GRI $= 0$ corresponds to a commensurate interface in the energetically most favorable stacking-mode, and GRI $= 1$ corresponds to a commensurate interface in the energetically most unfavorable stacking-mode. In the incommensurate case under study, all stacking modes are present

within the moiré superstructure, so that the GRI is expected to be very close to its average value of 0.5. Relaxation effects reduce this value as the contacting crystals minimize the energy by maximizing the regions of optimal stacking. At $\theta = 0^0$ we measured $GRI \sim 0.47$, which amounts to a ~ 6 % reduction with respect to $GRI = 0.5$, measured in the unrelaxed configuration. This reduction was found to be independent on temperature, clearly indicating that thermal fluctuations, which occur mostly in the vertical direction, do not wash out the overall interfacial matching. Further evidences are provided by the animations (see online Supplementary Information) showing the time evolution of the local registry patterns[17] and the out-of-plane displacements of the carbon atoms under sliding at various bath temperatures.

To conclude, we note that it would be more physically sound to consider a thick dynamic substrate and apply the thermostat to a finite portion of the substrate far from the interface to minimize its explicit effects on the dynamics of interest. This approach, however, considerably increases the computational burden making it essentially impractical for realistic model systems.[18]We note, however, that the fact that the result obtained at finite temperature only slightly differ from those obtained at 0 K suggests that the overall effect of thermal fluctuations is quite small and therefore the exact details of the application of the thermostat are of minor importance.

8. **Effects of Substrate Thickness**

In the main text, we reported results obtained using a minimal model of the interface, consisting of one mobile graphene layer sliding over a single rigid *h*-BN layer. To study the validity of this minimal model we performed more elaborate test simulations including thicker substrate models of up to five mobile *h*-BN layers supported by a fixed planar *h*-BN layer. The interlayer interactions between graphene and all the *h*-BN layers were computed using the heterogeneous graphene/*h*-BN interlayer potential,[19] while the interlayer interactions between different *h*-BN layers were computed adopting the homogeneous *h*-BN interlayer potential.[20] The intra-layer interactions within each *h*-BN monolayer were computed via the Tersoff potential as parameterized in Ref.[21].The intra-layer interactions within each graphene monolayer were computed using the REBO potential[14]. We considered three misfit angles of $\theta = 0^0, \sim 4^0$ and $\sim 24^0$, and constructed super-cells adopting the parameters reported in Table 1 of the Methods section of the main text. We notice here that the equilibrium boron-nitrogen bond-length distance of the intra-layer potential, $\mathrm{BN}_{\mathrm{Tersoff}} \simeq 1.44$ Å,

differs by $\Delta \simeq 0.02$ Å from that of the commensurate super-cells, $BN_{Supercell} \simeq 1.42$ Å. In order to avoid any residual stress, we implemented a rigid shift of all distances in the Tersoff potential, which allowed us to tune the equilibrium lattice spacing to the desired value (see Fig. S14a). We checked that the elastic properties of *h*-BN remained unchanged by comparing the phonon dispersion curves computed with our "shifted" potential, to those obtained adopting the original version (see Fig. S14b).

During the simulations, all *h*-BN layers were included in the dynamics, with the exception of the bottommost one, which was held fixed in the optimal planar crystalline configuration. For each thickness and misalignment, we first performed a geometry optimization. The final configurations were then used as starting points for the sliding friction simulations. These were done at zero temperature, $T = 0$ K, following the protocol outlined in Method section of the main text. Damping forces were applied to all mobile atoms in the system. If not otherwise specified, all simulation parameters are the same as those reported in the Methods section of the main text.

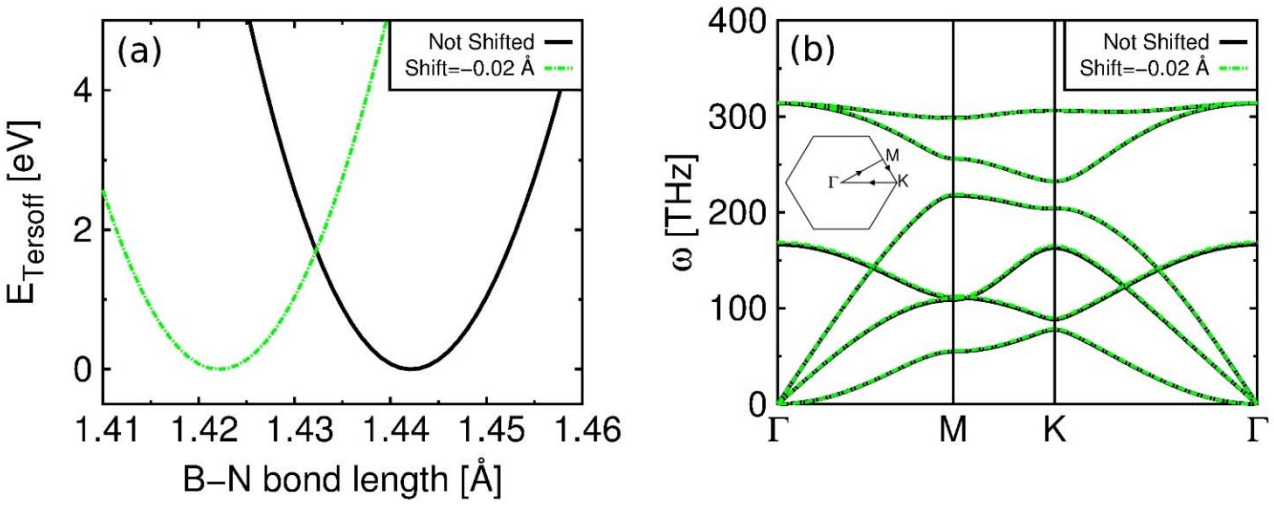

Figure S14: Implementation and test of the shifted Tersoff potential for the intra-layer interactions within a thick *h*-BN mobile substrate. Panel (a) shows the total energy curves as a function of the boron-nitrogen bond-length obtained with the original Tersoff potential of Ref.[21] (solid black curve) and after the implementation of a shift by $\Delta = 0.02$ Å of all the distances (green dotted-dashed curve). The overall result is a rigid shift that leaves the curvature unaffected. Panel (b) is a comparison between the phonon dispersion curves calculated with the two versions of the intra-layer potential, along the path in the Brillouin zone schematically reported in the inset. The differences are negligibly small, indicating that the implemented rigid shift does not affect the description of the intra-layer elastic properties of *h*-BN provided by the originally parameterized Tersoff potential.

Figure S15a reports the magnitude of the vertical out-of-plane distortions of the graphene layer $\left(\Delta z = \max_i(z_i) - \min_i(z_i)\right)$ as a function of the misfit angle θ for different substrate thicknesses. At small misfit angles ($\theta \lesssim 10^0$), increasing the substrate thickness is accompanied by an increase of the graphene layer corrugation. Specifically, at $\theta = 0^0$, Δz changes from ~ 0.21 Å in the rigid substrate model to ~ 0.38 Å in the largest model considered including five mobile substrate layers. We note here that the latter, though not necessarily converged, matches the experimentally observed corrugation of an aligned graphene monolayer over *h*-BN,[22] indicating that this model is sufficient in order to get a quantitative description of the static properties of the interface. At larger angles, $\theta > 10^0$, no significant changes are observed. The same picture applies to the distortions induced within each mobile substrate layer. This is shown in Fig. S15b, where we report Δz measured in each layer of the thickest model of the heterojunction at misfit angles of $\theta = 0^0$ and $\sim 24^0$. In the latter case, very small deformations $\left(\Delta z \simeq 0.01 \text{ Å}\right)$ are observed only within the two contacting layers of graphene and *h*-BN.

To investigate the contribution of the different layers to the frictional energy dissipation we plot in Fig. S15c the frictional power dissipated in each layer of the thickest model including five mobile *h*-BN layers at the aligned and $\theta \simeq 24^0$ rotated interfaces. In both cases dissipation is peaked in the contact region decaying rapidly away from the interface. The frictional power is found to decrease by one order of magnitude when going from the aligned to the misaligned junction, where graphene slides keeping a flat configuration that does not perturb much the underlying substrate.

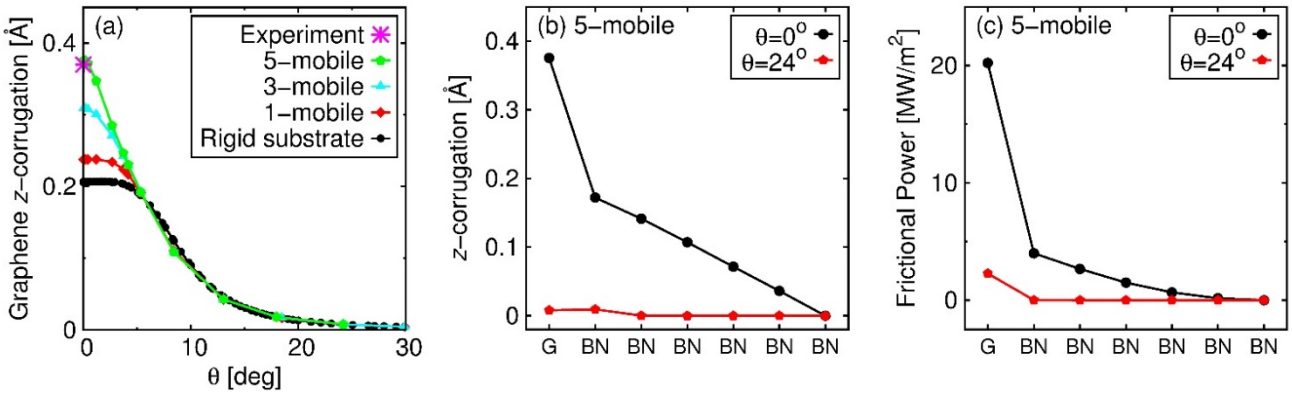

Figure S15: *h*-BN substrate thickness effects on the corrugation and frictional power of the heterogeneous graphene/*h*-BN interface. Panel (a) reports the magnitude of the out-of-plane distortions of graphene as a function of the misfit angle, θ, after relaxation over *h*-BN substrates of different thicknesses including up to five mobile layers. Panel (b) reports the magnitude of the out-of-plane distortions of each layer in the thickest models considered for the aligned and $\theta \simeq 24^0$ rotated interfaces. On the x axis, the label G indicates the graphene layer, while the labels BN indicate each *h*-BN layer. Panel (c) reports the corresponding frictional power dissipated under sliding.

Finally, Fig. S16a shows the average frictional stress as a function of misfit angle, θ, for increasing substrate thickness. As expected from the analysis of the surface corrugation and frictional power reported above, while at large misfit angles all the models give quantitatively similar results, for $\theta \lesssim 10^0$, friction is found to increase by a factor of ~4, when going from the minimal model to the thickest mobile substrate considered. This leads to an increase of the frictional anisotropy from ~4-fold to ~13-fold. We note, however, that in our simulations the value of the frictional anisotropy is controlled by the ratio $\eta_z/\eta_{x,y}$ between the out-of-plane and in-plane damping coefficients, the values of which have been roughly estimated based on atomic adsorption considerations (see Section 2.3 in Methods section of the main text). For example, by choosing a value of $\eta_z/\eta_{x,y} = 45$, threefold smaller than the one adopted in the main text $(\eta_z/\eta_{x,y} \sim 150)$, we reproduce the ~4-fold anisotropy observed in the experiments also in the thicker *h*-BN model with three mobile layers (see Fig. S16b).

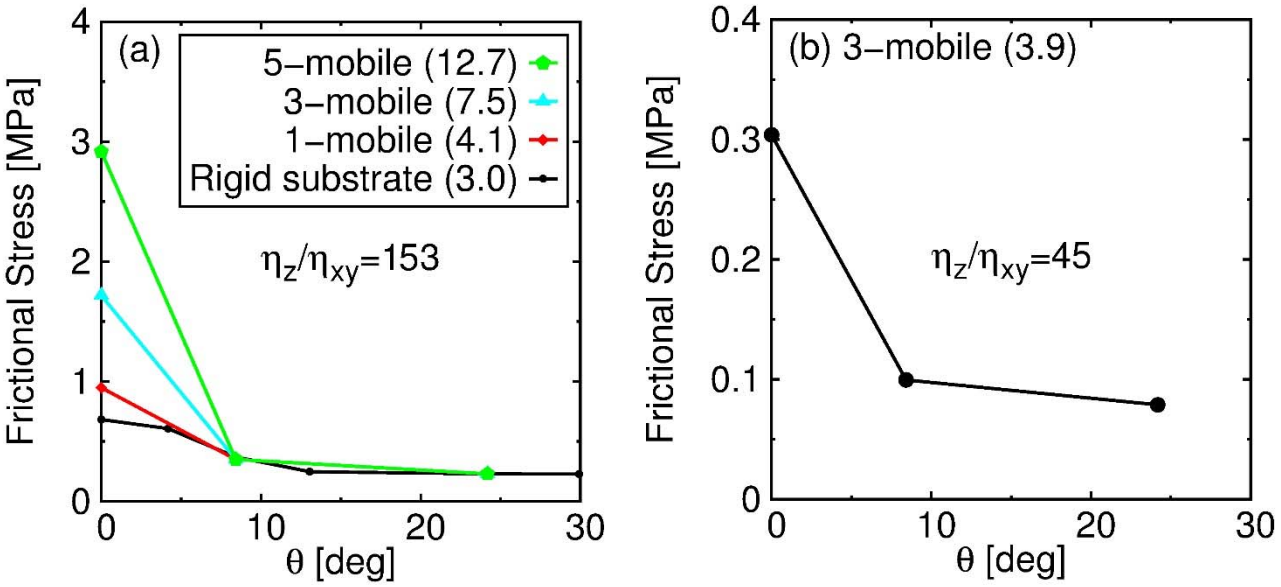

Figure S16: *h*-BN substrate thickness effects on the frictional stress of the heterogeneous graphene/*h*-BN interface. Panel (a) reports the average frictional stress as a function of the interfacial misfit angle, θ, measured for heterogeneous junctions including up to five mobile *h*-BN layers. Panel (b) reports the average frictional stress as a function of the interfacial misfit angle, θ, measured for a heterojunction model with 3 mobile *h*-BN layers adopting damping coefficients of $\eta_z = 0.45\ \mathrm{ps}^{-1}$ and $\eta_x = \eta_y = 0.01\ \mathrm{ps}^{-1}$, which yield the experimental ~4-fold frictional anisotropy. Numbers reported in round brackets in the captions correspond to the overall frictional anisotropy, calculated as the ratio between the frictional stresses measured at $\theta = 0^0$ and $\sim 24^0$.

To summarize this section, we find that upon inclusion of a mobile substrate the equilibrium relaxed structures reduce the overall system energy by increasing the interfacial adhesion. This is accompanied by an increase in the magnitude of the out-of-plane distortions of the interfacing graphene and *h*-BN layer. Correspondingly, the frictional stress under sliding is enhanced in comparison with the minimal model, mostly due to the corrugation of the heterojunction with minor contributions from frictional dissipation within the substrate itself. Importantly, these effects were found to be significant only at small misfit angles $\theta \lesssim 10^0$, becoming negligible at larger interfacial misalignments. Consequently, for a chosen set of damping coefficients $(\eta_z, \eta_{x,y})$ the overall frictional anisotropy is found to increase. Nevertheless, given our crude estimation of the damping coefficient one can readily find alternative physically viable values for these parameters, whose ratio will reproduce the experimentally measured frictional anisotropy. Therefore, while the inclusion of a mobile substrate provides a more realistic description of the system under study, the frictional

anisotropy is found to ultimately originate from the structural properties of the moiré superstructure of the heterogeneous interface. Since these features are well captured by the minimal model adopted in the main text, we conclude that it is sufficient to provide a consistent qualitative tribological description of the system.

9. **Description of the moiré Superstructure**

Figure S17 shows the relaxed structure of graphene over a rigid *h*-BN substrate, at various misfit angles, θ. A moiré pattern appears consisting of a periodic sequence of domains, where graphene stretches to adapt to the lattice constant of *h*-BN, separated by regions where in-plane compressive strain is accumulated (see top panels of Fig. S17). The relatively small bending rigidity of graphene allows for the partial relaxation of such compressive strain via the formation of elevated ridges, which reduce the total energy by converting energetically costly in-plane compressions into cheaper local out-of-plane distortions (see middle panels in Fig. S17). The bottom panels of Fig. S17 show the false color maps of the local registry index,[17] demonstrating how the stretched regions correspond to local realizations of the optimal C stacking-mode, that gradually turn into local realizations of the energetically more unfavorable A and A' stacking-modes at the elevated ridges regions.

Geometrically, the moiré superstructure can be described as a triangular lattice of periodicity $\lambda_{moiré}$, and angular orientation ψ, relative to the crystalline directions of the *h*-BN substrate. Both $\lambda_{moiré}$ and ψ are determined by the interface lattice mismatch, $\rho = a_{h-\mathrm{BN}}/a_g$, and misfit angle, θ. In particular, the moiré periodicity is given by[23] $\lambda_{moiré} = a_g/\sqrt{1+\rho^{-2}-2\rho^{-1}\cos\theta}$, while ψ satisfies $\cos\theta = \rho^{-1}\sin^2\psi + \cos\psi\sqrt{1-\rho^{-2}\cos\theta}$. As θ increases from zero to thirty degrees, the moiré periodicity rapidly shrinks and the superstructure rotates away from $\psi = 0°$. At the same time both the in-plane and out-of-plane distortions of graphene, which are the largest for the aligned contact, rapidly vanish (see Fig. S17), in agreement with the trend observed experimentally.[24] Due to the relatively weak interlayer interactions, the same qualitative picture should also apply to the interface formed between bulk graphite and bulk *h*-BN. Indeed, this has been verified by performing geometry optimizations of multilayer graphite relaxed atop a multilayer *h*-BN substrate.

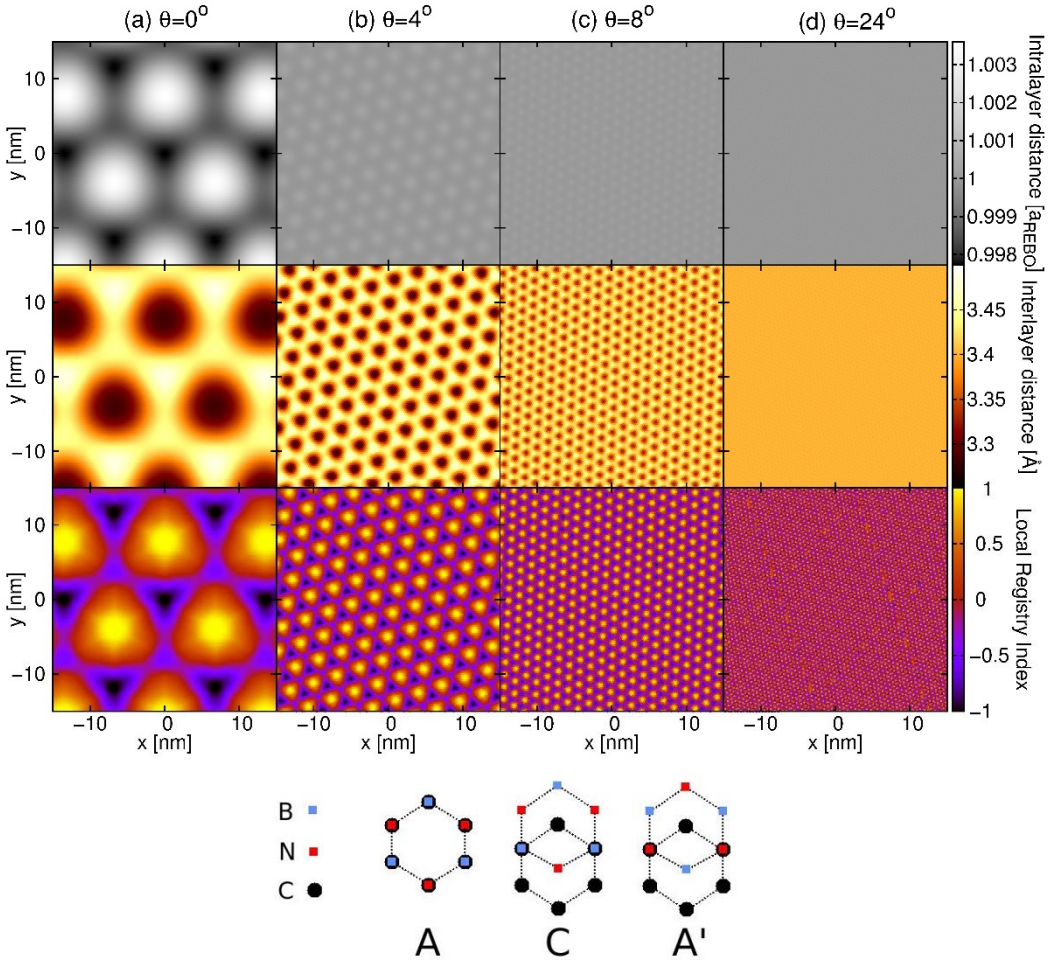

Figure S17: Moiré superstructure obtained for the heterogeneous graphene/*h*-BN interface at different misfit angles, θ. Panels in columns (a),(b),(c),(d) show the moiré super-structures obtained for graphene relaxed over a rigid *h*-BN layer at misfit angles of $\theta = 0^0, \sim 4^0, \sim 8^0$, and $\sim 24^0$, respectively. The color maps are obtained by plotting the equilibrium (x, y) positions of the carbon atoms in the relaxed graphene layer, colored according to the local average carbon-carbon (intra-layer) distance (top panels, presented in units of the equilibrium carbon-carbon distance of the isolated graphene layer), and the local (inter-layer) distance from the substrate (middle panels, in Å). The bottom panels show the local registry index,[17] where bright yellow corresponds to local realizations of the optimal C stacking-mode, whereas darker tones indicate the energetically less favorable A' (red/violet), and the least favorable A (black) stacking-modes. Several high symmetry stacking modes are schematically represented at the bottom of the figure.

10. Convergence of the Simulation Results with respect to Super-cell Size

The characteristic length scale of the heterogeneous contacts considered in this work is set by the periodicity, $\lambda_{\text{moiré}}$, of the moiré superstructure (see section S9 above). The size of the simulated super-cell should be sufficiently large with respect to $\lambda_{\text{moiré}}$ in order for the calculated static and

dynamic frictional properties of the interface to be converged. While this condition is generally satisfied at misalignment angles $\theta \gtrsim 4^0$, thanks to the rapidly decreasing value of $\lambda_{moiré}(\theta)$, that is not true in the super-cells adopted at small values of $\theta \sim 0^0$, where, moreover, the graphene equilibrium distortions are the largest (see Fig. S17). To check for finite size effects we therefore focus on the aligned geometry, $\theta = 0^0$, for which $\lambda_{\text{moiré}} \sim 136$ Å is the largest, and we performed tests adopting two different supercells of increasing size $L \simeq 136$ Å $\sim \lambda_{moiré}$ and $\simeq 269$ Å $\sim 2\lambda_{moiré}$, accommodating one and four moiré primitive cells, respectively. Both super-cells consist of one rigid *h*-BN substrate layer and one mobile graphene layer. The total number of carbon atoms in the cells are 6,272 and 24,642, respectively. We compare the surface corrugation (defined as the maximal amplitude of vertical carbon atoms displacements in the relaxed structure) and the calculated kinetic frictional stress under sliding at constant velocity of 10 m/s, and zero temperature ($T = 0$K). The surface corrugations obtained were 0.20604 and 0.20648 Å for the smaller and larger super-cells, respectively. The corresponding kinetic frictional stresses obtained were 0.687786 and 0.686650 MPa. These minor deviations (~ 0.2%) found for both properties indicate that finite size effects are sufficiently small in all the adopted simulation super-cells.

11. Comparison of the Graphene/*h*-BN Interlayer Potential and the Modified Kolmogorov-Crespi Potential

In the present study, we use our recently developed graphene/*h*-BN interlayer potential (ILP)[19] to describe the interlayer interactions between the *h*-BN substrate and the graphene slider. Recent related simulations used a modified Kolmogorov-Crespi (KC) potential,[15] parameterized to capture empirically observed out-of-plane corrugation in this system, to study the occurrence of a Novaco-McTague equilibrium misalignment angle.[25, 26] Since the graphene/*h*-BN ILP was carefully parameterized against state-of-the-art first-principle reference data, we believe that it provides a quantitative understanding of the experimentally observed frictional-stress anisotropy. To compare the performance of the two methods we plot in Fig. S18 the binding energy calculated for two different stacking modes of a stretched graphene/*h*-BN bilayer, where the lattice vectors of the two layers are taken to be identical (2.48 Å in length): (a) The A stacking mode, corresponding to the energetically least favored configuration, and (b) the C stacking mode, corresponding to the energetically most favorable configuration. The graphene/*h*-BN ILP nicely reproduces the reference

data from many-body dispersion augmented density functional theory (DFT+MBD) calculations for both stacking modes considered, with deviations smaller than 1 meV/atom and 0.02 Å for the binding energies and the equilibrium distances, respectively.[19, 27, 28, 29] The modified KC potential underestimates the binding energy by 3.5 meV/atom and overestimates the equilibrium distance by 0.10 Å, at the A stacking mode, whilst overestimating the binding energy by 3.2 meV/atom and underestimating the equilibrium distance by 0.14 Å, in the case of C stacking mode. In turn, these differences significantly affect the energetics and the geometrical properties of the infinite incommensurate contact.

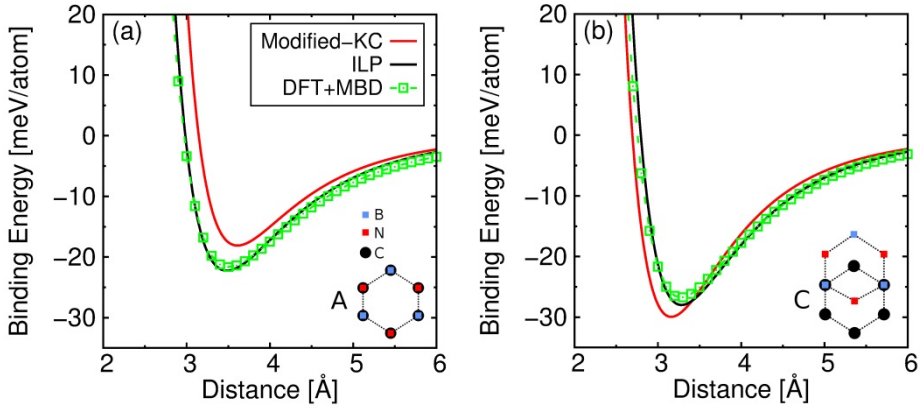

Figure S18: Comparison between the binding energies of the stretched graphene/*h*-BN bilayer calculated using the ILP[19] (black lines) and the modified KC potential [15] (red lines) at the (a) least energetically favorable and (b) optimal stacking modes (see insets). Green open squares represent the reference data obtained using the DFT+MBD approach.[19, 27, 28, 29] Reference energies were taken as the sum of individual layer contributions.

To further demonstrate the quantitative differences between the results obtained by the two force-fields we present in Fig. S19 the angular dependence of the adhesion energy and out-of-plane corrugation for the heterogeneous junctions studied in the present work. Notably, the graphene/*h*-BN ILP predicts overall larger adhesion energies with a ~5-fold smaller orientational anisotropy. Furthermore, the out-of-plane corrugation of the graphene layer obtained by the modified KC potential is consistently larger than that obtained by the graphene/*h*-BN ILP with differences of more than a factor 2 for the aligned case.

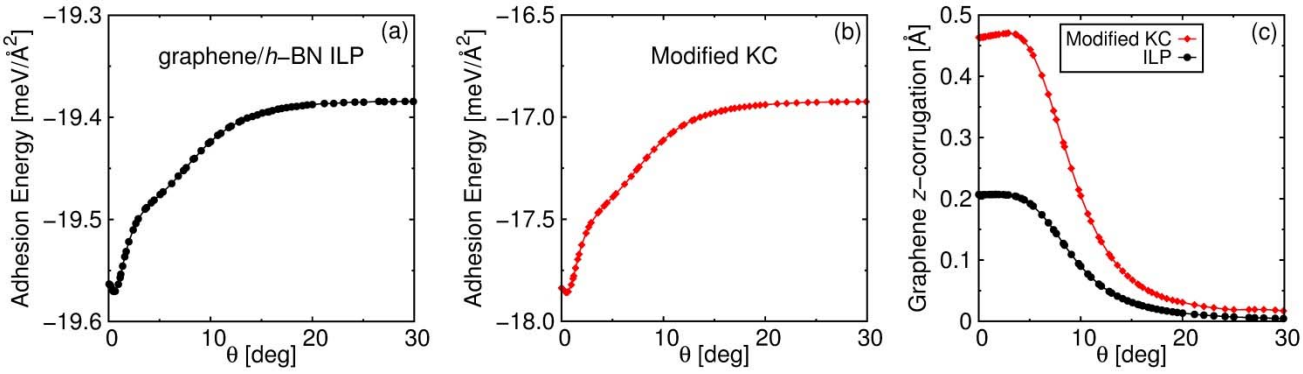

Figure S19: Comparison between the orientational dependence of the adhesion energies (panels (a) and (b)) and out-of-plane atomic corrugation (panel (c)) of graphene relaxed over a rigid *h*-BN layer calculated using the graphene/*h*-BN ILP[19] (black lines) and the modified KC potential (red lines).[15] Adhesion energies have been computed by subtracting the energy of isolated pristine graphene and *h*-BN layers from the total energy of the relaxed heterogeneous bilayer.

12. Parameters Used to Construct the Various Heterogeneous and Homogeneous Commensurate Super-Cells Discussed in the Main Text

Table S1: Parameters used to construct the simulated commensurate super-cells for the twisted heterogeneous graphene/*h*-BN junctions. The total number of atoms in each super-cell (N_P) is reported in the last column.

n_1	n_2	m_1	m_2	θ^0	ρ	a_{h-BN} (Å)	N_P
56	0	55	0	0	1.01818182	2.46508	12,322
26	41	21	44	4.18118152	1.01831159	2.46539	13,448
39	28	30	36	8.41931407	1.01830019	2.46537	13,346
32	45	15	57	13.04558814	1.01831235	2.46540	17,636
45	32	15	57	24.18019252	1.01831235	2.46540	17,636
61	56	3	98	29.91764859	1.01830427	2.46538	40,360

Table S2: Parameters used to construct the simulated commensurate super-cells for the twisted homogeneous graphene junctions. The total number of atoms in each super-cell (N_P) is reported in the last column.

n_1	n_2	m_1	m_2	θ^0	N_P
56	0	56	0	0	12,544
34	33	33	34	0.98743030	17,908
9	8	8	9	3.89023817	868
24	20	20	24	6.00898320	5,824
28	20	20	28	10.99273309	6,976
8	5	5	8	15.17817894	516
17	9	9	17	20.14658395	2,092
9	4	4	9	25.03965959	532
32	12	12	32	29.40931140	6,208

References

1. Cook SM, Lang KM, Chynoweth KM, Wigton M, Simmonds RW, Schäffer TE. Practical implementation of dynamic methods for measuring atomic force microscope cantilever spring constants. *Nanotechnology* 2006, **17**(9)**:** 2135-2145.
2. Sader JE, Chon JWM, Mulvaney P. Calibration of rectangular atomic force microscope cantilevers. *Review of Scientific Instruments* 1999, **70**(10)**:** 3967-3969.
3. Michalske TA, Tortonese M, Kirk M, Wendman MA. Characterization of application-specific probes for SPMs. 1997, **3009:** 53-60.
4. Haugstad G. *Atomic force microscopy: understanding basic modes and advanced applications*. John Wiley & Sons, 2012.
5. Koren E, Lortscher E, Rawlings C, Knoll AW, Duerig U. Surface science. Adhesion and friction in mesoscopic graphite contacts. *Science* 2015, **348**(6235)**:** 679-683.
6. Ogletree DF, Carpick RW, Salmeron M. Calibration of frictional forces in atomic force microscopy. *Review of Scientific Instruments* 1996, **67**(9)**:** 3298-3306.
7. Varenberg M, Etsion I, Halperin G. An improved wedge calibration method for lateral force in AFM. *Review of Scientific Instruments* 2003, **74**(7)**:**3362-3367.
8. Munz M. Force calibration in lateral force microscopy: a review of the experimental methods. *Journal of Physics D: Applied Physics* 2010, **43**(6)**:** 063001.
9. Li Q, Kim KS, Rydberg A. Lateral force calibration of an atomic force microscope with a diamagnetic levitation spring system. *Review of Scientific Instruments* 2006, **77**(6)**:**065105.
10. Saito R, Hofmann M, Dresselhaus G, Jorio A, Dresselhaus MS. Raman spectroscopy of graphene and carbon nanotubes. *Advances in Physics* 2011, **60**(3)**:** 413-550.
11. Ferrari AC, Basko DM. Raman spectroscopy as a versatile tool for studying the properties of graphene. *Nature nanotechnology* 2013, **8**(4)**:** 235-246.
12. Lee H, Lee HBR, Kwon S, Salmeron M, Park JY. Internal and External Atomic Steps in Graphite Exhibit Dramatically Different Physical and Chemical Properties. *ACS nano* 2015, **9**(4)**:** 3814-3819.
13. Hu H. ON THE EQUILIBRIUM OF A TRANSVERSELY ISOTROPIC ELASTIC HALF SPACE. *Science in China,SerA* 1954, **10**(3)**:** 463-479.
14. Brenner DW, Shenderova OA, Harrison JA, Stuart SJ, Ni B, Sinnott SB. A second-generation reactive empirical bond order (REBO) potential energy expression for hydrocarbons. *J Phys-Condens Mat* 2002, **14**(4)**:** 783-802.
15. van Wijk MM, Schuring A, Katsnelson MI, Fasolino A. Moire patterns as a probe of interplanar interactions for graphene on h-BN. *Phys Rev Lett* 2014, **113**(13)**:** 135504.
16. Leven I, Krepel D, Shemesh O, Hod O. Robust Superlubricity in Graphene/h-BN Heterojunctions. *J Phys Chem Lett* 2013, **4**(1)**:** 115-120.
17. Leven I, Guerra R, Vanossi A, Tosatti E, Hod O. Multiwalled nanotube faceting unravelled. *Nature nanotechnology* 2016, **11**(12)**:** 1082-1086.
18. Benassi A, Vanossi A, Santoro GE, Tosatti E. Parameter-free dissipation in simulated sliding friction. *Physical Review B* 2010, **82**(8)**:**081401.
19. Leven I, Maaravi T, Azuri I, Kronik L, Hod O. Interlayer Potential for Graphene/h-BN Heterostructures. *J Chem Theory Comput* 2016, **12**(6)**:** 2896-2905.
20. Leven I, Azuri I, Kronik L, Hod O. Inter-layer potential for hexagonal boron nitride. *The Journal of chemical physics* 2014, **140**(10)**:** 104106.
21. Sevik C, Kinaci A, Haskins JB, Çağın T. Characterization of thermal transport in low-dimensional boron nitride

nanostructures. *Physical Review B* 2011, **84**(8)**:**085409.

22. Li X, Lu X, Li T, Yang W, Fang J, Zhang G*, et al.* Noise in Graphene Superlattices Grown on Hexagonal Boron Nitride. *ACS nano* 2015, **9**(11)**:** 11382-11388.
23. San-Jose P, Gutiérrez-Rubio A, Sturla M, Guinea F. Spontaneous strains and gap in graphene on boron nitride. *Physical Review B* 2014, **90**(7)**:**075428.
24. Woods CR, Britnell L, Eckmann A, Ma RS, Lu JC, Guo HM*, et al.* Commensurate–incommensurate transition in graphene on hexagonal boron nitride. *Nature Physics* 2014, **10**(6)**:** 451-456.
25. Novaco AD, McTague JP. Orientational Epitaxy—the Orientational Ordering of Incommensurate Structures. *Physical Review Letters* 1977, **38**(22)**:** 1286-1289.
26. Guerra R, van Wijk M, Vanossi A, Fasolino A, Tosatti E. Graphene on h-BN: to align or not to align? *Nanoscale* 2017, **9**(25)**:** 8799-8804.
27. DiStasio RA, Jr., von Lilienfeld OA, Tkatchenko A. Collective many-body van der Waals interactions in molecular systems. *Proceedings of the National Academy of Sciences of the United States of America* 2012, **109**(37)**:** 14791-14795.
28. Ambrosetti A, Reilly AM, DiStasio RA, Jr., Tkatchenko A. Long-range correlation energy calculated from coupled atomic response functions. *The Journal of chemical physics* 2014, **140**(18)**:** 18A508.
29. Kronik L, Tkatchenko A. Understanding molecular crystals with dispersion-inclusive density functional theory: pairwise corrections and beyond. *Accounts of chemical research* 2014, **47**(11)**:** 3208-3216.